

The vortex-Nernst effect in a superconducting infinite-layer nickelate

Nicholas P. Quirk¹, Danfeng Li^{2,3}, Bai Yang Wang^{2,4}, Harold Y. Hwang^{2,3}, and N. P. Ong^{1,§}

¹*Department of Physics, Princeton University,
Princeton, NJ 08544, USA*

²*Stanford Institute for Materials and Energy Sciences,
SLAC National Accelerator Laboratory,
Menlo Park, California 94025, USA*

³*Department of Applied Physics,
Stanford University, Stanford, CA 94305, USA*

⁴*Department of Physics, Stanford University,
Stanford, CA 94305, USA*

(Dated: September 7, 2023)

We report measurements of the Nernst and Seebeck effects in $\text{Nd}_{1-x}\text{Sr}_x\text{NiO}_2$ thin films near the superconducting transition temperature, $T = 6.5 - 15$ K. Our main result is the observation of a vortex-Nernst signal $S_{yx}(T, H)$ with a maximum at $\mu_0 H = 5$ T and a tail that extends to $\mu_0 H \approx 15$ T, which we identify as the upper-critical field H_{c2} . At $T > T_c = 6.1$ K, H_{c2} remains large (15 T), up to the highest temperature we can resolve from S_{yx} (11 K). These results indicate the existence of a vortex-liquid state over a wide range of finite-resistance temperatures, as in the high- T_c cuprates.

INTRODUCTION

The discovery of superconductivity in hole-doped infinite-layer nickelates has drawn many comparisons to the high- T_c cuprate superconductors [1–12]. Despite fundamental differences, e.g., the parent state of the cuprates is an antiferromagnetic insulator whereas the parent compounds of the nickelates are metals, the two systems share multiple clear similarities. Most notably, both have a broad superconducting dome that is flanked by Fermi-liquid behavior on the overdoped side and poor conductivity (a correlation-driven resistivity upturn in the nickelates) on the underdoped side [13].

A hallmark of cuprate superconductors is the evidence for vortex-like fluctuations of the superconducting order parameter that extend to temperatures T well above the resistive critical temperature T_c [16]. Above T_c , the vortex liquid state persists to temperatures as high as 100 K above T_c in underdoped $\text{La}_{2-x}\text{Sr}_x\text{CuO}_4$ (LSCO) and $\text{YBa}_2\text{Cu}_3\text{O}_{6+y}$ (YBCO). This unusual behavior was discovered through Nernst [16–20] and torque magnetometry measurements of the diamagnetic response [21–26], which can detect the vortex-liquid state with high sensitivity. The rapid diffusion of the vortices leads to loss of phase rigidity in the condensate above T_c .

To sharpen the comparison between the two systems, we have investigated the vortex-Nernst effect in $\text{Nd}_{1-x}\text{Sr}_x\text{NiO}_2$ near T_c (6.5 - 15 K). We have also measured the low-temperature Seebeck effect which probes the particle-hole asymmetry in the normal-state density of states $\mathcal{N}(E)$. In a thermal gradient $-\nabla T \parallel \hat{\mathbf{x}}$ and a magnetic field $\mathbf{H} \parallel \hat{\mathbf{z}}$, the observed electric field \mathbf{E} in the x - y plane defines the thermoelectric matrix S_{ij} , viz. $E_i = S_{ij}(-\partial_j T)$. The diagonal component S_{xx} corresponds to the Seebeck effect (or thermopower) whereas

the off-diagonal component yields the Nernst response

$$S_{yx}(T, H) = E_y/|\nabla T|. \quad (1)$$

Here the observed field profile of S_{yx} is strongly non-linear in H , displaying a broad maximum at $\mu_0 H \approx 5$ T and a long tail that extends to 15 T. (Although our maximum field is 13 T, we estimate by extrapolation that the vortex signal vanishes at ~ 15 T.) In an optimally doped sample ($x = 17.5\%$), $S_{yx}(5 \text{ T})$ falls from 290 nV/K at 6.5 K to less than 20 nV/K (below the noise floor of our experiment) at 15 K, concurrently with the onset of the normal-state resistance. However, $H_{c2}(T)$ does not vanish at T_c . A similar trend occurs in a second sample with 20% hole doping. From these results, we infer that vortex-like fluctuations exist in a temperature interval above T_c , but the interval is smaller than in underdoped cuprates. We caution, however, that our results are taken on samples with known structural disorder and inhomogeneity [1, 13] which could substantially reduce the extent of the vortex liquid. It is possible that the Nernst response may extend to higher temperatures in improved films, such as those grown on $(\text{LaAlO}_3)_{0.3}(\text{Sr}_2\text{TaAlO}_6)_{0.7}$ substrates [13], which warrants further investigation.

METHODS

Thin $\text{Nd}_{1-x}\text{Sr}_x\text{NiO}_2$ films (of thickness 9-11 nm) were grown on $2.5 \times 5 \text{ mm}^2$ SrTiO_3 substrates by pulsed-laser deposition and capped with a 2 nm-thick SrTiO_3 top layer. (See Ref. [1] for thin-film growth details.) We consider two samples with Sr concentration $x = 17.5\%$ (Sample A, optimally doped) and 20% (Sample B, overdoped). In Sample A, the resistive transition begins at 15 K and reaches zero resistance at 6.1 K. The resistance

is 10% of its normal-state value at $T_{c,10\%R} = 7.7$ K. The T_c in Sample B is lower, occurring between 3 and 13 K; $T_{c,10\%R} = 5.3$ K. Under an applied temperature gradient, the base temperature reachable in our experiment is ~ 6.5 K—slightly above the zero-resistance temperature of each sample (Fig. 1c).

Electrical characterization measurements were conducted with standard lock-in techniques using aluminum wire-bonded contacts. The thermoelectric DC voltages were probed by phosphor-bronze wires connected with silver paint to the aluminium bonds and soldered to pads on the cold-finger of a custom high-vacuum probe with all-copper wiring to room temperature. The voltages were read out by a Keithley 2182a nanovoltmeter. The temperatures were measured by two RuO₂ thermometers attached to the sample by thick gold wires using silver epoxy. These thermometers were calibrated *in situ* in zero magnetic field using a Cernox CX-1010 thermometer which has very low magnetoresistance in this temperature range. The magnetic field was swept at ≤ 0.2 T/min.

A temperature gradient $-\nabla T \parallel \hat{\mathbf{x}}$ was generated in the sample using a 1 k Ω thin-film resistor mounted to one end of the crystal with silver paint. The opposite end of the sample was glued to a brass stage on the cold-finger using GE varnish (Fig. 1a). A major challenge in the experiment is posed by the feeble Nernst response (maximum Nernst voltage $V_N \sim 300$ nV). The large thermal conductance of the SrTiO₃ substrate severely limits the temperature gradient, especially above 15 K. The use of sensitive thermometers as well as a pulsed measurement technique to remove offsets and drift in the DC voltages allowed us to overcome some of these difficulties (Fig. 1b). A current pulse lasting $\tau \approx 40$ s was applied to the heater to establish a stable $-\nabla T$. The longitudinal (Seebeck) and transverse (Nernst) voltage drops were measured after stabilization. The heater was then turned off and the sample was allowed to relax for time τ . The DC voltages were again measured and these were subtracted from the previous values in order to record the true thermoelectric voltage responses. The sample temperature and temperature gradient were recorded as the average of and difference between the two thermometers during the energized part of the cycle.

RESULTS AND DISCUSSION

Figure 2 depicts low-temperature magnetotransport measurements on the optimally doped film (Sample A, $x = 17.5\%$). In the normal state ($T > 13$ K), the Hall coefficient is -2.7×10^{-4} cm²/C, in agreement with previous measurements [11]. Below $T = 6.5$ K, both the transverse (Hall) resistivity ρ_{yx} and longitudinal resistivity ρ_{xx} are zero up to an onset magnetic field: $H_m(T)$ in ρ_{xx} and $H_v(T)$ in ρ_{yx} . Magnetic fields stronger than

$H_m(T)$ induce melting of the vortex solid. Rapid motion of vortices in the liquid state produce a finite $\mathbf{E} = \mathbf{B} \times \mathbf{v}$ observed as a finite flux-flow resistivity ρ_{xx} and flux-flow Hall resistivity ρ_{yx} (\mathbf{B} is the flux density and \mathbf{v} the velocity of the vortex core). We plot these onset magnetic fields in the T - H phase diagram depicted in Figure 5c.

We have measured the thermoelectric matrix S_{ij} in Nd_{1-x}Sr_xNiO₂ in the vicinity of the superconducting regime. In the normal state, the zero- H Seebeck coefficient $S_{xx}(T) = E_x/|\nabla T|$ is proportional to $(dN/dE)_\mu$, the derivative of the density of states $\mathcal{N}(E)$ evaluated at the chemical potential μ . The Nernst response is comprised of two distinct contributions. The quasiparticle (or carrier) contribution S_{yx}^{qp} is distinguished by its H -linear field profile at moderate H whereas the vortex-Nernst term S_{yx}^{v} has a characteristic non-monotonic field profile. By additivity, we have

$$S_{yx} = S_{yx}^{\text{qp}} + S_{yx}^{\text{v}}. \quad (2)$$

In this system, the short quasiparticle mean-free-path ℓ makes $S_{yx}^{\text{qp}} \ll S_{yx}^{\text{v}}$ in general [17, 20]. However, when the vortex-Nernst contribution vanishes (at $T > 13$ K), S_{yx}^{qp} is readily resolved. When Cooper-pair correlations become large, phase slippage induced by moving vortices produces a dominant vortex-Nernst contribution S_{yx}^{v} which displays the characteristic tilted-dome field profile [20] shown in Fig. 4a.

Figure 3 shows the results of the Seebeck experiment on Sample A (Figs. 6a, b for Sample B). In the normal state, $T \geq 13$ K, the zero-field Seebeck coefficient $S_{xx}(T, 0)$ is a negative constant: -1.2 $\mu\text{V}/\text{K}$ (-0.5 $\mu\text{V}/\text{K}$) in Sample A (B). The negative sign of S_{xx} agrees with that of the Hall coefficient (Fig. 2a). As T is lowered below 15 K, $|S_{xx}|$ decreases monotonically, approaching zero at 6.5 K. The application of a perpendicular magnetic field H suppresses superconductivity and increases $|S_{xx}|$ (Sample A: Fig. 3a; Sample B: Fig. 6a).

To address the vortex-Nernst response in the vicinity of T_c , we distinguish between two types of fluctuations of the complex superconducting order parameter $\hat{\Psi}$. Gaussian (or amplitude) fluctuations correspond to fluctuations of the modulus $|\hat{\Psi}|$ about the minimum of the Ginzburg-Landau potential well. In a conventional type-I superconductor (Al and Sn), Gaussian fluctuations are restricted to a very narrow interval above T_c (of width $\delta T \sim 10^{-2} T_c$).

The second class of fluctuations (called ‘‘singular’’) are produced by mobile vortices in the vortex-liquid state in type-II superconductors. In a driving temperature gradient $-\nabla T$, the passage of each vortex across the line joining the transverse ‘‘Hall’’ contacts causes the Josephson phase φ between the contacts to wind by 2π [16–20]. For a vortex flow rate \dot{N}_v in the low-density limit (where N_v is the number of vortices), the Hall contacts detect the Josephson voltage $V_j = 2\pi(\hbar/e)\dot{N}_v$, which accounts

for the vortex-Nernst signal V_N in weak H (vortex cores are well-separated). The slope of the initial H -linear increase defines the Nernst coefficient, viz.

$$\nu(T) = \lim_{H \rightarrow 0} S_{yx}(T, H)/H. \quad (3)$$

When S_{yx}^v is dominant, the initial H -linear dependence reflects the insertion of vortices by the external field which leads to a proportionate increase of V_N with net vorticity. With increasing H , however, the vortex-Nernst response increasingly deviates downwards from the initial H -linear growth because of the decrease in $|\mathbf{v}|$ in large H and the progressive weakening of the condensate amplitude $|\hat{\Psi}|$. Eventually, as $H \rightarrow H_{c2}$, V_N approaches zero [20].

In conventional 3D type-II superconductors (e.g. Nb and NbSe₂), the vortex liquid in the T - H plane is confined between the vortex-solid melting curve $H_m(T)$ and the upper critical field $H_{c2}(T)$ (Fig. 5a). In the BCS scenario $H_{c2}(T)$ vanishes linearly with the reduced temperature $t = 1 - T/T_c$ as we approach T_c from below. Hence, in the T - H plane, the two curves $H_m(T)$ and $H_{c2}(T)$ converge to the point $(T_c, 0)$ as $t \rightarrow 0$. Above T_c , the vortex signal vanishes rapidly as a weak, evanescent tail in accord with the vanishing of $|\hat{\Psi}|$ at T_c .

Fluctuations in hole-doped cuprate superconductors are categorically different from the BCS (mean-field) scenario [16, 20, 21, 25, 26]. Below T_c (as measured by resistivity ρ) the vortex liquid remains bounded from below by the melting curve $H_m(T)$ (Fig. 5b). However, the upper boundary $H_{c2}(T)$ has eluded accurate measurement (with estimates varying from 100 T to 300 T). A striking feature is that, as we approach T_c from below, we never observe the curve $H_{c2}(T)$ approaching zero in *any* of the hole-doped cuprates [20, 25]. Instead, the vortex-liquid state is observed to extend well above T_c to temperatures as high as 160 K. These unexpected observations have led to the conclusion that, in the hole cuprates, the amplitude $|\hat{\Psi}|$ remains finite well above T_c [20, 21, 25, 26]. The abrupt onset of finite ρ at T_c actually corresponds to the vanishing of phase rigidity and the emergence of the vortex-liquid state; the Cooper condensate remains stable above T_c but is strongly phase disordered. Aside from the Nernst evidence, this scenario is confirmed by measurements of the diamagnetic response using torque magnetometry [21–23, 25, 26]. A closely related observation is that the superconducting energy gap Δ measured in tunneling experiments persists at the same value to temperatures well above T_c (instead of closing) while the subgap region is progressively filled in. With this perspective in mind, we examine the situation in the infinite-layer nickelate.

The key result in our report is Figure 4a which shows the field profiles of the observed Nernst response $S_{yx} = E_y/|\nabla T|$ at various temperatures T above T_c in the optimally doped sample (Sample A). Most of the curves

feature the characteristic tilted-dome profile [20]. As H increases, the initial H -linear form in weak H evolves to a broad maximum near 5 T, finally followed by a gradual monotonic decrease on the large- H side. As discussed, the field at which the tilted-dome profile ends nominally indicates where the condensate amplitude vanishes [20, 21, 25, 26]. This provides an estimate of the upper critical field H_{c2} .

However, if the quasiparticle contribution S_{yx}^{qp} is finite (see Eq. 2), we need to subtract off S_{yx}^{qp} before estimating H_{c2} [17]. The H -linear field profile of $S_{yx}(T, H)$ measured at 15.03 K (lowest-lying curve in Fig. 4a) suggests that it is predominantly comprised of S_{yx}^{qp} .

This is confirmed by examining the T dependence of the Nernst coefficient ν (Eq. 3) plotted in Fig. 4c. At $T = 6.5$ K (just above T_c), ν is observed to have the rather large value 180 nV/KT. As T is raised above T_c , ν decreases very steeply but saturates (at ~ 13 K) to a small finite value (~ 10 nV/KT). The observed behavior supports our identification of the curve of S_{yx} at 15.03 K in Fig. 4a with the quasiparticle contribution S_{yx}^{qp} . The onset temperature of the vortex Nernst signal is estimated as $T_{\text{onset}} \simeq 13$ K.

Hence, subtracting the curve of $S_{yx}(H)$ at 15.03 K from the other curves at lower T in Fig. 4a isolates the field profile of the vortex Nernst signal. At a selected temperature T' , we estimate $H_{c2}(T')$ as the field at which the curves of S_{yx} measured at T' and at 15.03 K intersect.

Similar features are obtained in Sample B (Fig. 6c, d).

We note that estimates of the upper critical field based on the resistive transition (which we call H_{c2}^R here) show that $H_{c2}^R(T)$ approaches zero as $T \rightarrow T_c$ [14, 15] instead of the T -independent profile in Fig. 5c. The resistive transition actually measures the collapse of phase rigidity caused by melting of the vortex solid, which leads to dissipation, whereas the vortex Nernst signal detects the existence of the pair condensate. In a mean-field superconductor, both should agree. However, when phase rigidity vanishes in relatively weak H , they strongly disagree. This is the situation in hole-doped cuprates and appears to be the case here as well.

VORTEX-LIQUID STATE

From the results in Sample A, we derive the phase diagram shown in Figure 5c. The onset field of dissipation measured by the resistivity $\rho_{xx}(T, H)$, which we define to be the melting field $H_m(T)$ is plotted as black squares. The onset field H_v of the vortex Hall effect $\rho_{yx}(T, H)$ is plotted as blue circles. At each T , the relation $H_v(T) > H_m(T)$ implies that melting of the vortex solid initially leads to the diffusive motion of vortices that cause ρ_{xx} to be finite. However, the core velocity \mathbf{v} becomes large enough to produce a finite ρ_{yx} only when H exceeds the higher $H_v(T)$. The relation $H_v(T) > H_m(T)$

was previously observed in $2H\text{-NbSe}_2$ [27]. For comparison, we also plot the profile of the zero- H resistivity ρ vs. T (dashed curve).

The comparison implies that the zero-field dissipationless state that emerges at T_c (6.1 K) is readily suppressed in a weak H . The most instructive plot is $H_{c2}(T)$ (blue triangles) inferred from S_{yx}^v in Fig. 4a. We find that $H_{c2}(T)$ remains at the same value (~ 15 T) even as T exceeds T_c . As mentioned, the vortex-Nernst contribution to the coefficient ν remains finite until 13 K (Fig. 4c). Together, the three curves $H_m(T)$, $\nu(T)$ and $H_{c2}(T)$ imply that the entire dissipative region shaded in blue is actually a vortex-liquid state that persists to $T_{\text{onset}} \simeq 13$ K, well above T_c (6.1 K). The ratio $T_{\text{onset}}/T_c \simeq 2$ is comparable to values obtained in optimally and overdoped $\text{La}_{2-x}\text{Sr}_x\text{CuO}_4$. This implies that the transition at T_c also corresponds to a loss of phase rigidity of the pair condensate rather than closing of the gap $\Delta(T)$. Based on this conclusion, we anticipate that $\Delta(T)$ should not close at T_c but remain finite up to 13 K as a pseudogap whose subgap states are progressively occupied.

In the present samples, the resistive transition is quite broad. This suggests that the films may be comprised of domains with a broad distribution of condensate strengths as reflected by the individual T_c 's. However, we do not expect a broad distribution to affect our argument supporting a vortex-liquid state based on the curves in Fig. 4a. A distribution of superconducting domains, each following the BCS scenario (Fig. 5a), will still display an $H_{c2}(T)$ curve that approaches zero at the highest T_c , in conflict with our observation.

Recently, optimally doped $\text{Nd}_{1-x}\text{Sr}_x\text{NiO}_2$ grown on LSAT substrates have been shown to have higher crystalline quality than the present films grown on SrTiO_3 [13]. The resistive transitions are considerably sharper with the T -linear resistivity profile persisting nearly to T_c . Nernst measurements on the improved samples should allow us to determine how T_{onset} varies with doping.

[1] D. Li, K. Lee, B. Y. Wang, M. Osada, S. Crossley, H. R. Lee, Y. Cui, Y. Hikita, and H. Y. Hwang, *Nature* **572**, 624 (2019).
 [2] K-W. Lee and W. E. Pickett, *Phys. Rev. B* **70**, 165109 (2004).
 [3] A. S. Botana and M. R. Norman, *Phys. Rev. X* **10**, 011024 (2020).
 [4] H. Sakakibara, H. Usui, K. Suzuki, T. Kotani, H. Aoki, and K. Kuroki, *Phys. Rev. Lett.* **125**, 07703 (2020).
 [5] Y. Xiang, Q. Li, Y. Li, H. Yang, Y. Nie, and H. H. Wen, *Chinese Phys. Lett.* **38**, 047401 (2021).
 [6] W. Sun, Y. Li, R. Liu, J. Yang, J. Li, W. Wei, G. Jin, S. Yan, H. Sun, W. Guo *et al.*, *Adv Mater.* **35**, e2303400 (2023).
 [7] N. N. Wang, M. W. Yang, Z. Yang, K. Y. Chen, H.

Zhang, Q. H. Zhang, Z. H. Zhu, Y. Uwatoko, L. Gu, X. L. Dong *et al.*, *Nature Commun.* **13**, 4367 (2022).
 [8] Q. Gao, Y. Zhao, X. Zhou, and Z. Zhum, *Chinese Phys. Lett.* **38**, 077401 (2021).
 [9] G. A. Pan, D. Ferenc Segedin, H. LaBollita, Q. Song, E. M. Nica, B. H. Goodge, A. T. Pierce, S. Doyle, S. Novakov, D. Córdova Carrizales *et al.*, *Nature Mater.* **21**, 160 (2022).
 [10] M. Osada, B. Y. Wang, B. H. Goodge, S. P. Harvey, K. Lee, D. Li, L. F. Kourkoutis, and H. Y. Hwang, *Adv. Mater.* **33**, 2104083 (2021).
 [11] D. Li, B. Y. Wang, K. Lee, S. P. Harvey, M. Osada, B. H. Goodge, L. F. Kourkoutis, and H. Y. Wang, *Phys. Rev. Lett.* **125**, 027001 (2020).
 [12] S. Zeng, C. S. Tang, X. Yin, C. Li, M. Li, Z. Huang, J. Hu, W. Liu, G. J. Omar, H. Jani *et al.*, *Phys. Rev. Lett.* **125**, 147003 (2020).
 [13] K. Lee, B. Y. Wang, M. Osada, B. H. Goodge, T. C. Wang, Y. Lee, S. Harvey, W. J. Kim, Y. Yu, C. Murthy *et al.*, *Nature* **619**, 7969 (2023).
 [14] B. Y. Wang, D. Li, B. H. Goodge, K. Lee, M. Osada, S. P. Harvey, L. F. Kourkoutis, M. R. Beasley, and H. Y. Hwang, *Nat. Phys.* **17**, 473 (2021).
 [15] B. Y. Wang, T. C. Wang, Y. T. Hsu, M. Osada, K. Lee, C. Jia, C. Duffy, D. Li, J. Fowlie, T. P. Devereaux *et al.*, *Sci. Adv.* **9**, eadf6655 (2023).
 [16] Z. Xu, N. P. Ong, Y. Wang, T. Kakeshita, and S. Uchida, *Nature* **406**, 486 (2000).
 [17] Y. Wang, Z. A. Xu, T. Kakeshita, S. Uchida, S. Ono, Y. Ando, and N. P. Ong, *Phys. Rev. B* **64**, 224519 (2001).
 [18] Y. Wang, N. P. Ong, Z. A. Xu, T. Kakeshita, S. Uchida, D. A. Bonn, R. Liang, and W. N. Hardy, *Phys. Rev. Lett.* **88**, 257003 (2002).
 [19] Y. Wang, S. Ono, Y. Onose, G. Gu, Y. Ando, Y. Tokura, S. Uchida, and N. P. Ong, *Science* **299**, 86 (2003).
 [20] Y. Wang, L. Li, and N. P. Ong, *Phys. Rev. B* **73**, 024510 (2006).
 [21] Y. Wang, Lu Li, M. J. Naughton, G. Gu, S. Uchida, and N. P. Ong, *Phys. Rev. Lett.* **95**, 247002 (2005).
 [22] L. Li, Y. Wang, M. J. Naughton, S. Ono, Y. Ando, and N. P. Ong, *Europhys. Lett.* **72**, 451 (2005).
 [23] L. Li, Y. Wang, J. G. Checkelsky, M. J. Naughton, S. Komiya, S. Ono, Y. Ando, and N. P. Ong, *Physica C* **49**, 460 (2007).
 [24] D. C. Johnston and J. H. Cho, *Phys. Rev. B* **42**, 8710 (1990).
 [25] L. Li, Y. Wang, S. Komiya, S. Ono, Yoichi Ando, G. D. Gu, and N. P. Ong, *Phys. Rev. B* **81**, 054510 (2010).
 [26] F. Yu, M. Hirschberger, T. Loew, G. Li, B. J. Lawson, T. Asaba, J. B. Kemper, T. Liang, J. Porras, G. S. Boebinger *et al.*, *Proc. Nation. Acad. Sci.* **113**, 12667 (2016).
 [27] T. W. Jing and N. P. Ong, *Phys. Rev. B* **42**, 10781 (1990).

[§]Corresponding author email: npo@princeton.edu

Acknowledgement We thank Kyuho Lee for helpful discussions. We acknowledge support of the U.S. National Science Foundation through grant DMR 2011750. Work at Stanford/SLAC was supported by the Department of Energy, Office of Basic Energy Sciences, Division of Materials Sciences and Engineering, under contract no. DE-AC02-76SF00515.

Author contributions

NPQ, NPO and HYH conceived the idea for the exper-

iment. Samples were grown and characterized by DL, BYW, and HYH. NPQ performed all the measurements and wrote the text with NPO and inputs from all authors.

Competing financial interests

The authors declare no competing financial interests.

Correspondence and requests for materials should be addressed to N.P.Q. or N.P.O.

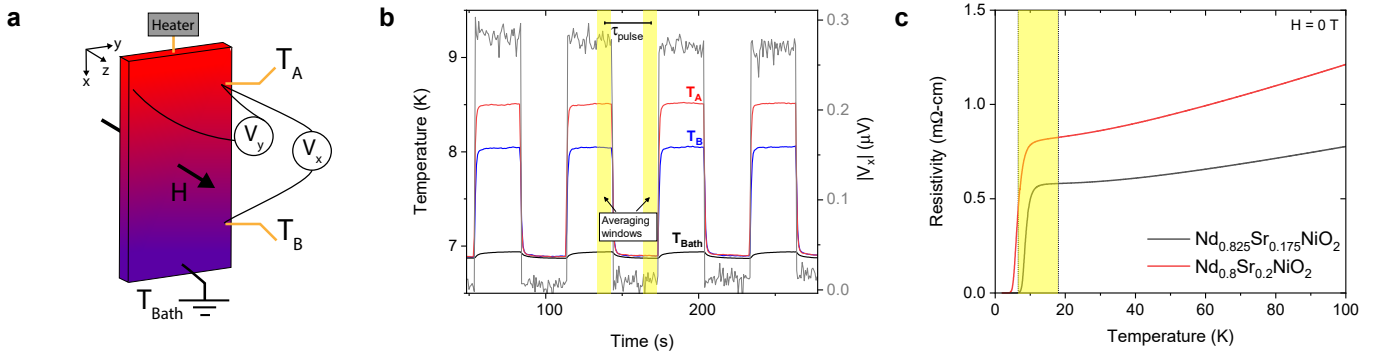


FIG. 1. **Experimental set-up.** **a.** Schematic of the Seebeck/Nernst experiment. A resistive heater fixed to the top end of the sample generates a temperature gradient $-\nabla T \parallel \hat{x}$ that is measured by two RuO_2 thermometers $T_{A,B}$. The Seebeck response is calculated from the resulting longitudinal DC voltage V_x and the Nernst from V_y . The magnetic field H is directed perpendicular to the a - b plane ($\parallel \hat{z}$). **b.** DC offsets and drifts are removed with a pulsed measurement technique. The heater is energized for a time τ_{pulse} , longer than the equilibration time between the sample and the temperature bath T_{bath} , about 40 seconds. The voltage is recorded as the difference in the stabilized signals (yellow averaging windows) of the off/on stages of the cycle. **c.** Zero-field resistivity versus temperature of the two nickelate films. Sample A (Sr = 17.5%, optimally doped) is shown in black and Sample B (Sr = 20%) in red. The yellow window highlights the temperature range accessible to our Nernst/Seebeck experiments.

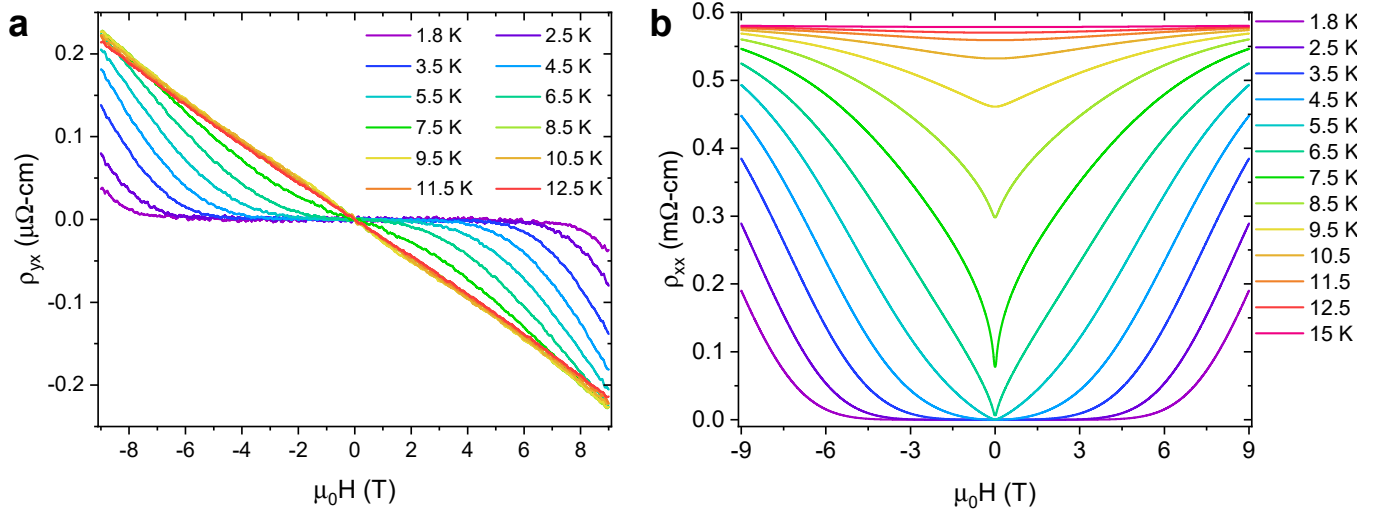


FIG. 2. **Magnetotransport ($H \parallel \hat{z}$).** Hall effect (a) and magnetoresistance (MR) (b) in the optimally doped film, Sample A (Sr = 17.5%). The sample reaches zero resistance at $T_c \approx 6.1$ K. We extract the vortex-solid melting field, $H_m(T)$ from the onset of non-zero MR (b) and the onset field of the vortex-Hall effect $H_v(T)$ from the appearance of non-zero $\rho_{yx}(H, T)$ (a). These onset fields are plotted in Fig. 5c.

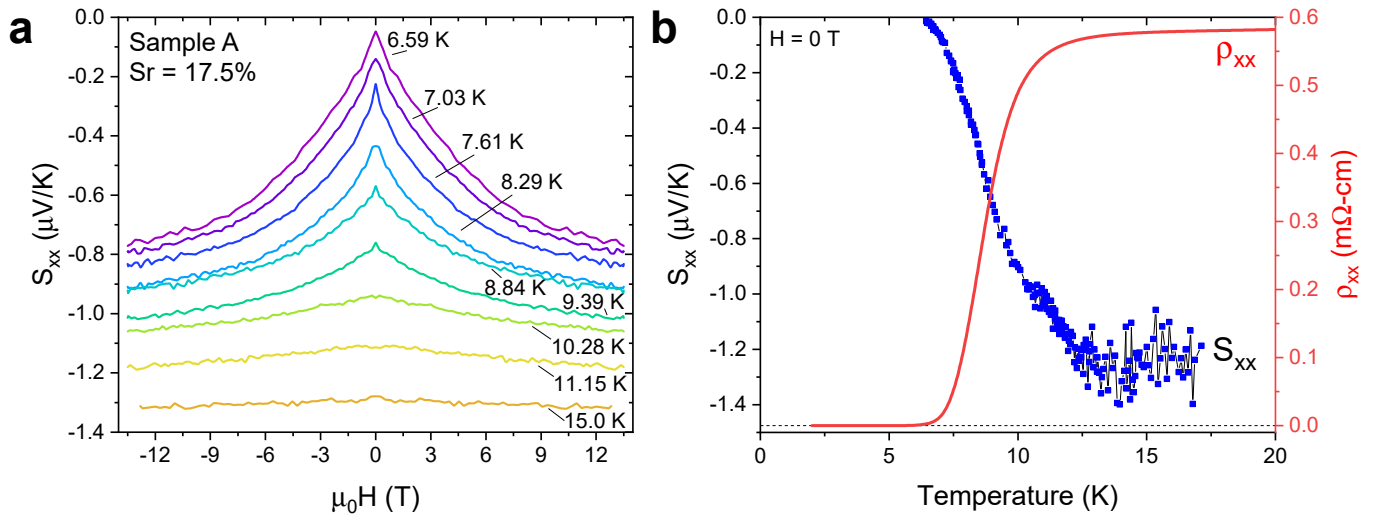


FIG. 3. Seebeck effect in $\text{Nd}_{0.825}\text{Sr}_{0.175}\text{NiO}_2$. **a.** Magnetic field sweeps of the Seebeck coefficient $S_{xx}(H, T)$ at fixed temperature. **b.** $S_{xx}(0, T)$ plotted alongside the zero-field resistivity (ρ_{xx}). S_{xx} reaches zero concurrently with the onset of the zero-resistivity state at T_c .

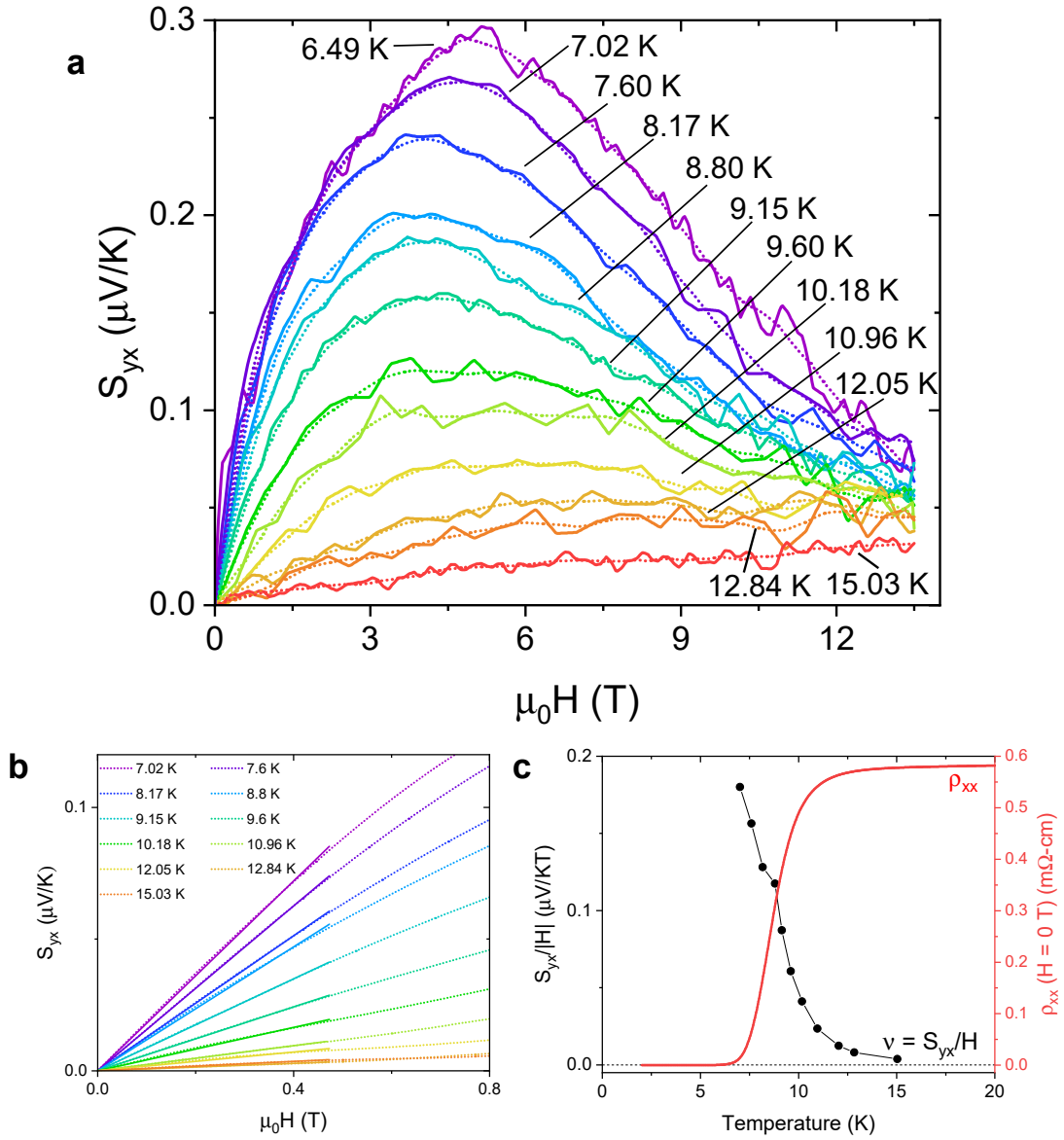


FIG. 4. **Vortex-Nernst effect in $\text{Nd}_{0.825}\text{Sr}_{0.175}\text{NiO}_2$.** **a.** Field sweeps of the Nernst response $S_{yx}(H, T)$ at fixed temperatures. The solid-line curves are the field-antisymmetrized raw data and the dotted lines have Savitsky-Golay smoothing added. **b.** The low-field (≤ 0.5 T) linear fits used to extract ν in **b**. The dotted lines are the smoothed S_{yx} data shown in **a**. **c.** This shows the temperature dependence of the Nernst coefficient $\nu = S_{yx}/H$ alongside the zero-field resistivity. The Nernst coefficient falls below 10 nV/KT at $T > 13$ K.

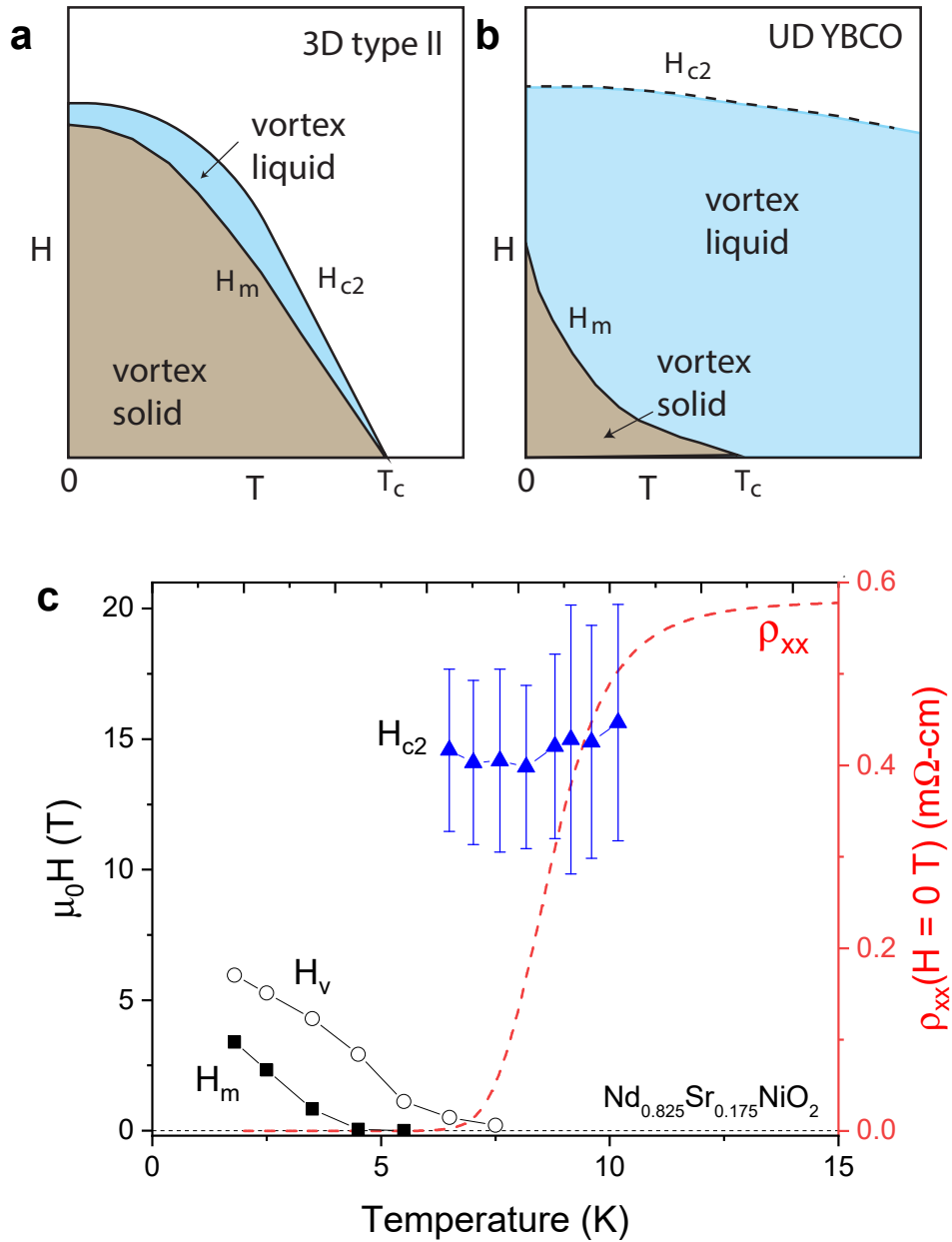


FIG. 5. **Comparison of the BCS, underdoped cuprate, and infinite-layer nickelate T - H phase diagrams.** **a.** The standard BCS phase diagram in the T - H plane for a 3D type-II superconductor. The vortex solid (grey) is stable below the melting field $H_m(T)$. The vortex liquid (blue) is confined between $H_m(T)$ and the upper critical field $H_{c2}(T)$. $H_{c2}(T)$ decreases to zero linearly in $(T_c - T)$. **b.** The phase diagram in an underdoped cuprate (e.g. $\text{YBa}_2\text{Cu}_3\text{O}_y$ ($y \sim 6.6$) [26]). The melting field $H_m(T)$ shows pronounced positive curvature vs. T and terminates at T_c . The upper critical field $H_{c2}(T)$ (dashed curve) is estimated to lie well above 50 T. At T_c , H_{c2} remains very large. **c.** The T - H phase diagram for the infinite-layer nickelate inferred from the vortex-Nernst effect in Sample A. The lowest curve (solid squares) plots the onset of dissipative behavior in $\rho_{xx}(H)$ which we identify with $H_m(T)$. The field at which ρ_{yx} becomes finite ($H_v(T)$) is shown as open circles. The upper critical fields $H_{c2}(T)$ inferred from high-field linear fits to $S_{yx}(T, H)$ (Fig. 4a) are plotted as blue triangles. The error bars represent the propagation of one standard deviation in the linear fit of $S_{yx}(T = 15 \text{ K}, H > 9 \text{ T})$ subtracted from that of $S_{yx}(T, H > 9 \text{ T})$. We infer that the nickelate vortex-liquid state exists in the region bounded above by $H_{c2}(T)$ and below by $H_m(T)$. Note the poor signal-to-noise ratio in $S_{yx}(H, T > 11 \text{ K})$ precludes us from estimating $H_{c2}(T > 11 \text{ K})$.

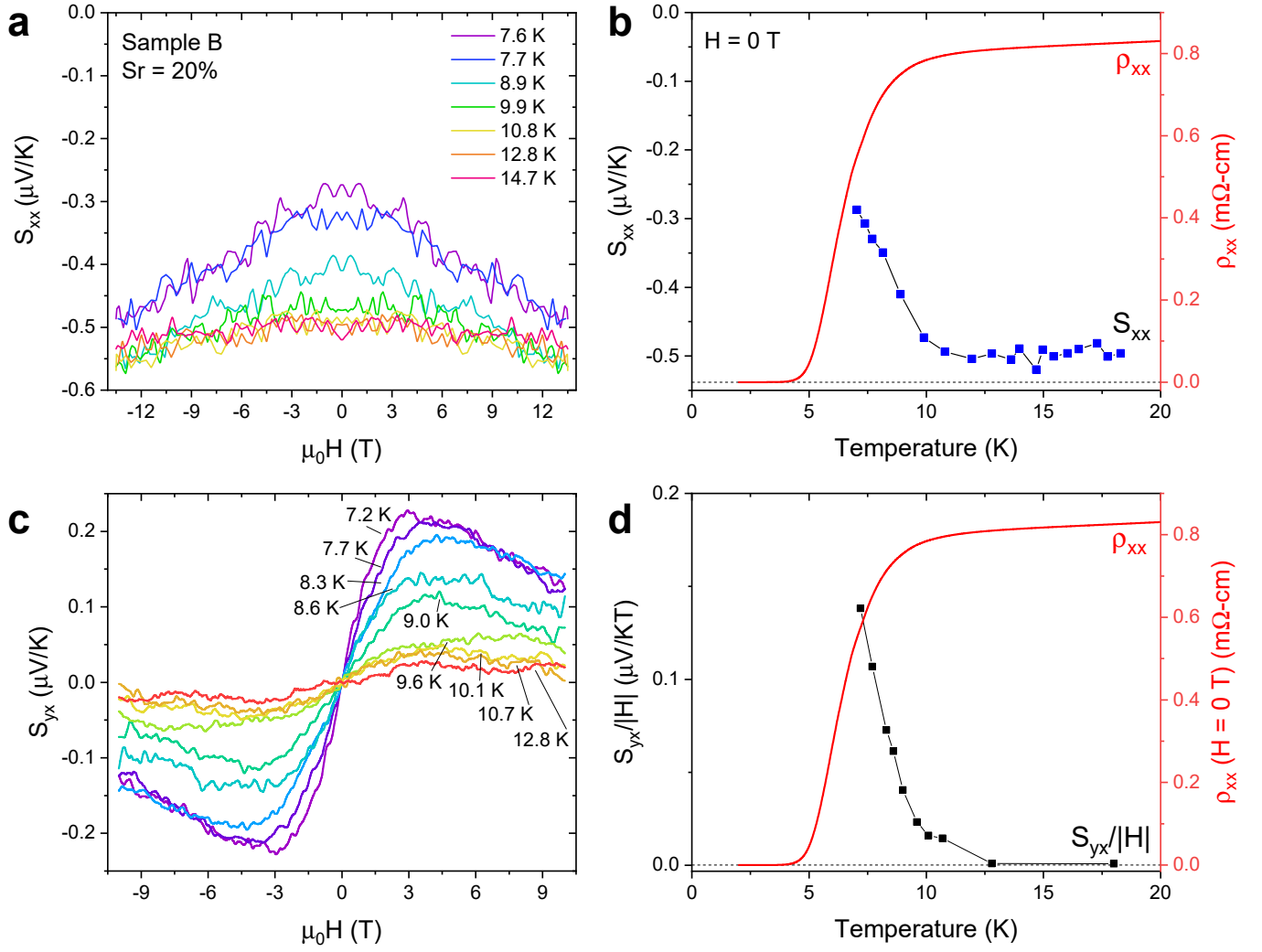


FIG. 6. Seebeck and Nernst effects in $\text{Nd}_{0.8}\text{Sr}_{0.2}\text{NiO}_2$ (Overdoped). **a**. Field sweeps of the Seebeck coefficient $S_{xx}(H, T)$ at fixed temperature. **b**. Temperature dependence of $S_{xx}(H = 0, T)$, plotted alongside the zero-field resistivity (ρ_{xx}). In the normal state, $T = 12 - 18$ K, $S_{xx}(H = 0, T)$ has a constant value of -0.5 $\mu\text{V/K}$. **c**. Field sweeps of the Nernst response $S_{yx}(H, T)$ at fixed temperatures. **d**. The temperature dependence of the Nernst coefficient $\nu = S_{yx}/H$, plotted with the zero-field resistivity (ρ_{xx}). S_{yx}/H vanishes by $T \approx 13$ K.